Applied Catalysis B: Environmental 257 (2019) 117929

Contents lists available at ScienceDirect

Applied Catalysis B: Environmental

journal homepage: www.elsevier.com/locate/apcatb

Elucidation of Fe-N-C electrocatalyst active site functionality via in-situ X-ray absorption and operando determination of oxygen reduction reaction kinetics in a PEFC

Luigi Osmieri[a], Rajesh K. Ahluwalia[b], Xiaohua Wang[b], Hoon T. Chung[c], Xi Yin[c], A. Jeremy Kropf[b], Jaehyung Park[b], David A. Cullen[d], Karren L. More[d], Piotr Zelenay[c], Deborah J. Myers[b], K.C. Neyerlin[a,*]

[a] National Renewable Energy Laboratory, Golden CO, 80401, USA
[b] Argonne National Laboratory, Lemont IL, 60439, USA
[c] Los Alamos National Laboratory, Los Alamos NM, 87545, USA
[d] Oak Ridge National Laboratory, Oak Ridge TN, 37830, USA

ARTICLE INFO

Keywords:
Fe-N-C catalyst
Polymer electrolyte fuel cell
Reaction order
Activation energy
Modeling

ABSTRACT

In the past decade the notable effort placed on improving intrinsic electrochemical kinetics of platinum group metal (PGM)-free electrocatalysts for the oxygen reduction reaction (ORR) has led to a significant improvement in both performance and understanding of this class of electrocatalysts. However, a limited amount of this development and understanding has been undertaken using operando electrochemical diagnostics at the membrane electrode assembly (MEA) level. In this work, the operando ORR kinetics on an atomically dispersed iron-nitrogen-carbon ((AD)Fe-N-C) PGM-free electrocatalyst have been examined to extract the reaction order and the activation energy of the ORR. The experiments were carefully designed to ensure the stability/predictability of the electrocatalyst during the data collection process and thus validate the relevance of the values obtained for the aforementioned parameters. A kinetic model that considers a potential-dependent availability of active sites (θ) is proposed. Active site availability is shown to be a function of both the change in the oxidation state (n_R) and the redox potential at which the metal center transitions from a higher oxidation state to a lower one (). The resulting model fitting parameters for n_R and (0.71 and 0.788 V, respectively) obtained from the analysis of operando data correlate well with those from *in situ* X-ray absorption near edge structure measurements (n_R = 0.57) and *in situ* cyclic voltammetry measurements (0.75 V < < 0.8 V) in the MEA environment. The resulting model provides an excellent fit of MEA performance across the range of pressures, temperatures, and potentials under which the data were collected.

1. Introduction

Polymer electrolyte fuel cells (PEFCs) are electrochemical devices that directly convert the chemical energy of a fuel (most often hydrogen) into electrical energy. The high efficiency of this energy conversion, together with the emission of only water, if H_2 is produced using renewable energy, make PEFCs an attractive technology for clean energy applications. In addition, PEFC operating temperatures are close to ambient conditions such that start-up and shutdown are quick. All these features make the PEFC an attractive candidate to replace internal combustion engines for powering vehicles [1–3].

Unfortunately, PEFCs also have several challenges hindering their widespread application in the automotive sector. One of the main drawbacks is their high cost, mainly dictated by the use of Pt (a costly and rare noble metal) to catalyze both the anodic hydrogen oxidation reaction (HOR) and the cathodic oxygen reduction reaction (ORR) [4]. Due to the slower kinetics of the ORR compared to the HOR, the Pt loading in a PEFC is considerably higher on the cathode than on the anode [5–7]. Thus, an enormous amount of research effort has been dedicated to reducing the Pt cathode loading and to replacing Pt with a less costly, platinum group metal-free (PGM-free), earth-abundant material.

The fundamental understanding of PGM-based electrocatalysts has improved as a result of several decades of research dedicated to

* Corresponding author.
E-mail address: kenneth.neyerlin@nrel.gov (K.C. Neyerlin).

https://doi.org/10.1016/j.apcatb.2019.117929
Received 26 February 2019; Received in revised form 1 June 2019; Accepted 5 July 2019
Available online 09 July 2019
0926-3373/ © 2019 Published by Elsevier B.V.

Nomenclature

α_C	Cathodic transfer coefficient, product of symmetry factor and the number of electrons transferred in the rate determining step, -
β	Symmetry factor (assumed equal to 0.5 for ORR), -
γ	Reaction order for ORR with respect to O_2 partial pressure at constant overpotential, -
ζ	Correction factor for H^+ resistance in the cathode accounting for catalyst layer utilization, -
η_A	Anode kinetic overpotential (assumed negligible), V
η_C	Cathode kinetic overpotential, V
θ	Fraction of active site availability/activity, -
E_C	*i*R-free cell potential, observed cell voltage plus corrections for high-frequency resistance and proton resistance in the cathode catalyst layer, V
E_c^0	Cathode potential vs SHE, V
E_{corr}	iR-free cell potential corrected for thermodynamic contributions of p_{H_2} and p_{O_2}, V vs. SHE
E_{cell}	Measured cell potential, V
E_{rev}	Reversible cell potential (function of T, p_{H_2}, and p_{O_2}), V
E_{rev}^0	Reversible cell potential in the reference conditions of 25 °C and $p_{O_2} = p_{H_2} = 1$ atm (1.23 V), V vs. SHE
E_R^0	Potential of the reversible redox couple for the distribution of ORR active sites, V vs. SHE
$E_{HFR-free}$	HFR-free cell voltage, observed cell voltage plus correction from high-frequency resistance, V
F	Faraday constant, C mol^{-1}
ΔH_C	Activation energy of the ORR determined at zero overpotential, kJ mol^{-1}
i	current density, A cm^{-2}
$i_{0,T^*}^{\theta=1}$	Catalyst electrode exchange current density at full active site availability/activity at T*, function of p_{O_2}, A cm^{-2}
$i_{0,p_{O_2}^*}^{\theta=1}$	Catalyst electrode exchange current density at full active site availability/activity at $p_{O_2}^*$, function of T, A cm^{-2}
i_0^*	Catalyst electrode exchange current density at full active site availability/activity (function of electrode loading, active site density and activity distribution), defined at the reference conditions of $p_{O_2} = 1$atm, T = 80°C, A cm^{-2}
n	Number of electrons transferred in the ORR rate determining step (assumed equal to 1 for ORR), -
n_R	Effective change of Fe oxidation state for the distribution of ORR active sites, -
p_{H_2}	H_2 partial pressure, atm
$p_{H_2}^*$	Reference H_2 partial pressure (1atm), atm
p_{O_2}	O_2 partial pressure, atm
$p_{O_2}^*$	Reference O_2 partial pressure (1atm), atm
R	Universal gas constant, J $mol^{-1}K^{-1}$
R_{sheet}	Cathode electrode sheet resistance, Ω cm^2
R_Ω^C	H^+ resistance in the cathode catalyst layer; obtained from EIS using a transmission line model, Ω cm^2
R_Ω^{HFR}	High frequency resistance of the cell; comprised of membrane protonic and cell electronic bulk and contact resistances, Ω cm^2
R_Ω^m	Ohmic resistance of the membrane, Ω cm^2
R_Ω^e	Sum of cell bulk electronic and contact resistance, Ω cm^2
T	Temperature, K
T^*	Reference state temperature (80°C), K

understanding the ORR mechanism and its limitations. This research has utilized systems ranging from single crystals to dispersed Pt-based electrocatalysts measured using rotating disk electrodes (RDE) [8–13], and single PEFC membrane-electrode assemblies (MEAs) [5,14–16]. While PGM-free ORR catalysts have also been the subject of intensive research for over half a century [2,3,17–19], the heterogeneous nature of these materials has limited the depth of the knowledge of the active site and the ORR mechanism versus that of the PGM electrocatalysts. To that end, several consortia focused on PGM-free electrocatalyst / electrode development for PEFCs were recently established to enable a more integrated and comprehensive analysis of PGM-free-based MEAs [20–22].

For PGM-based electrocatalysts, MEA-level operando studies have enabled the determination of relevant ORR kinetic parameters (*i.e.*, reaction order, activation energy, and exchange current density), which has improved the understanding of potential-driven phenomena, such as the impact of Pt oxide coverage as well as the identification, assessment, and subsequent improvement of both proton and local Pt transport losses [16,23–30]. Despite the increasing interest and recent developments in the field of PGM-free ORR catalysis, similar systematic efforts to obtain operando kinetic information have not yet been undertaken. This may in part be due to the variety of PGM-free catalysts (stemming from a variety of synthesis precursors and approaches) [3,17–19], the resulting distribution of electrochemically- active site turnover frequencies and chemical compositions [18,31,32], difficulty in clearly identifying the precise ORR active site(s) [33,34], and most critically, the inability to obtain steady-state performance data [35–37].

A majority of recent studies have come to a consensus that the ORR active sites in materials derived from a transition metal precursor and a source of carbon and nitrogen, such as a carbon-nitrogen-based polymer (e.g., polyaniline) or metal-organic framework, are comprised of an ionized transition metal atom (*e.g.*, Fe, Co, Mn) coordinated by N, embedded in a carbonaceous matrix [38–42]. Assuming that these N-coordinated ionized transition metal atoms act as the ORR active site(s), various research groups have tried to elucidate the relationship between active site availability and the resulting kinetics. One observation that has been repeatedly reported is the concomitant positions of the redox peak, obtained from cyclic voltammetry, and the ORR onset potential [43–46]. This correlation has been probed by investigating the aforementioned electrochemical characteristics of various Fe-based PGM-free electrocatalysts [47,48].

In this regard, the theory of the “asymmetric volcano” trend was proposed [39,49]. Here, the redox potential of the N-coordinated transition metal atoms was related to the ORR onset potential and the intrinsic ORR activity in terms of turn over frequency (TOF) and O_2 binding energy [39,49]. RDE results have shown a good agreement with this theory, indicating that the transition metal itself, along with its coordination and incorporation in the catalyst’s carbonaceous matrix, play a fundamental role in properly catalyzing the ORR [50–53]. However, while RDE is a powerful investigative tool, it suffers from certain fundamental limitations, namely low dissolved O_2 concentration in the aqueous electrolyte, which limit the ability to acquire critical information at high current density and low cell potential [54]. Hence, it becomes evident that any experiment designed to probe the electrochemical performance across a wide range of potential and current density must be done in an operating PEFC. While operando kinetics have been measured previously for Pt-based catalysts [15,16], to the best of our knowledge such a comprehensive study does not yet exist for PGM-free catalysts.

Recent efforts in PGM-free catalysts development at Los Alamos National Laboratory have yielded a relatively robust atomically dispersed iron ((AD)Fe-N-C) [55,56] PGM-free ORR catalyst, with polarization curves exhibiting little variation within a several hour-long test window.

In this work, we leveraged the limited degradation of the (AD)Fe-N-C electrocatalyst to enable the collection of operando kinetic

information, producing, for the first time, MEA-level kinetic parameters (exchange current density, reaction order, activation energy, and active site(s) availability) for a PGM-free electrocatalyst. The operando data was utilized in combination with *in situ* X-ray absorption near edge structure (XANES) experiments in an MEA to produce a better understanding of PGM-free active site availability/activity as a function of both cathode potential and the change in oxidation state for atomically-dispersed Fe-based PGM-free electrocatalysts, elaborating on previously proposed active site availability models [39,43,57]. The resulting PGM-free kinetic model produced an excellent fit of the experimental data over the complete range of O_2 pressure, temperature, and cell potential for which the experimental data are available.

2. Results and discussion

2.1. Physicochemical characterization

The as-synthesized (AD)Fe-N-C catalyst consists of rod-shaped carbon structures with a length typically between 1.5–2.0 µm and a width of about 0.2 µm (see low magnification SEM in Fig. 1a). Higher magnification SE- and HAADF-STEM images of the same rod have previously shown the presence of micro- and mesoporosity distributed within the rod structure [55]. The lack of mesopores observed on the rods surface in SE images compared to the plethora of mesopores observed in the HAADF-STEM images indicates that the mesopores exist within the rod core and are likely due to the evaporation of Zn during heat treatment [53,58,59].

The presence of atomically dispersed Fe atoms within and at the edges of graphitic carbon domains is evident in Fig. 1b (individual bright spots). Electron energy loss spectra were previously acquired with the electron probe positioned on both individual atoms and the support, illustrating the concomitant detection of N (K-edge) and Fe (L-edge) [55].

This is clear evidence that the atomically dispersed Fe atoms are surrounded by N for this (AD)Fe-N-C catalyst. Similar results have been reported in recent studies of Fe-N-C based PGM-free ORR catalysts [38,40]. The evidence for the association of Fe and N in these materials provides clear experimental evidence that the ORR active site structure widely proposed in the literature, *e.g.*, Fe atom centers coordinated with nitrogen (Fe-N_x) [34,60–64], is actually present in this PGM-free catalyst.

Fig. 1 (a) SEM images illustrating the rod-shape and (b) high-resolution HAADF-STEM, showing atomically dispersed Fe atoms (individual bright spots) for the as-synthesized AD(Fe)-**N**-C catalyst.

Secondary-electron images of cross-sections of the hand painted (AD)Fe-N-C based MEAs are shown in Fig. 2. Here, Fig. 2a shows the entire MEA cross-section of the Pt/C anode, Nafion N211 membrane, and (AD)Fe-N-C cathode electrode. From this image, the cathode catalyst layer ranged in thickness between 75 and 90 µm. Figs. 2b and 2c illustrate the homogeneity of both the catalyst content/distribution and the electrode porosity. Assuming a packing density for the catalyst of 0.4 g cm^{-3} [5], this electrode thickness corresponds well with a nominal catalyst loading of *ca.* 3.8 mg cm^2 deposited on the cathode. The porous structure of the cathode catalyst layer, as well as the typical rod shape of the (AD)Fe-N-C catalyst particles, are also evident in Fig. 2c-d. The red outlined region in Fig. 2d indicates a macropore between the carbon rods, while EDS spectrum images of the same electrode area are displayed in Fig. 2e. Here, the ionomer (indicated by the F-rich (green) regions of the image) appears evenly distributed throughout the cathode, although the ionomer does exhibit highly aggregated regions, as does the electrocatalyst (indicated by the blue regions denoting C) and the macropores (indicated by the **black** regions).

Fig. 2 (a) Cross-section SEM image of MEA showing Pt/C anode catalyst layer (top), N211 membrane, and (AD)Fe-N-C cathode catalyst layer (bottom). (b)-(c) SEM images at different magnification showing details of cathode catalyst layer structure. (d) HAADF-STEM image of cathode catalyst layer cross-section. (e) Fluorine and carbon overlaid EDS map of same area shown in (d). The red outline in (d) and (e) mark an example of a macropore.

2.2. MEA tests results

The first objective of this work was to develop a methodology to systematically investigate operando ORR kinetics. In order to do so, however, one must consider that historically one of the major limitations to the acquisition of operando information has been the rapid degradation of electrode/electrocatalyst performance [35–37]. Needless to say, such poor stability strongly affects the reliability of the experimental data along with any subsequent understanding that can be gleaned from the application of a kinetic model.

To that point, a preliminary test was conducted on one MEA (MEA #0 in Fig. 3a), to evaluate both a suitable cell break-in procedure and to identify a period over which stable, predictable and repeatable performance could be achieved, both within a single MEA test and between multiple MEAs. To examine the time dependent performance, the MEA was held at 0.40 V, at 80 °C, under H_2/O_2 at 100% RH and 1.5 atm, while the current density was recorded. A cell potential of 0.40 V was chosen for two main reasons. First, according to a recent durability study conducted on a similar Fe-N-C PGM-free catalyst at the MEA level, it was found that holding the potential at high values produced a faster degradation of the catalyst performance than at low potentials [65]. Second, holding the cell at a sufficiently low potential and a correspondingly higher current density, allowed for the generation of water and heat, the combination of which may help to fully hydrate and activate the membrane and the ionomer in the catalyst layer [7,29]. While it is acknowledged that the variability of PGM-free catalysts in terms of both the chemical precursors and synthesis methods [3] could indeed lead to different requirements for the activation or break-in

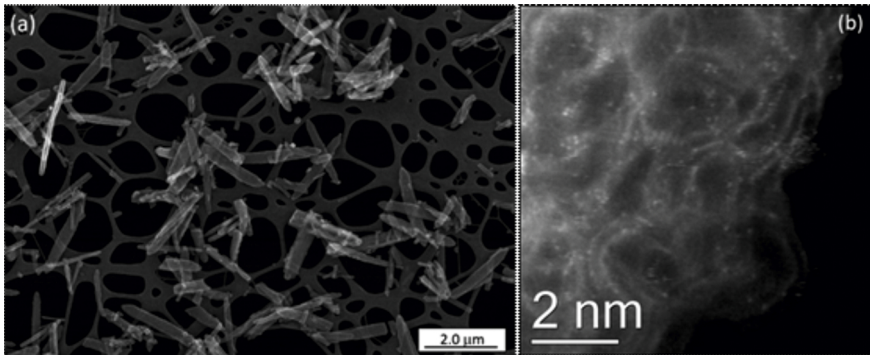

Fig. 1. (a) SEM images illustrating the rod-shape and (b) high-resolution HAADF-STEM, showing atomically dispersed Fe atoms (individual bright spots) for the as-synthesized AD(Fe)-N-C catalyst.

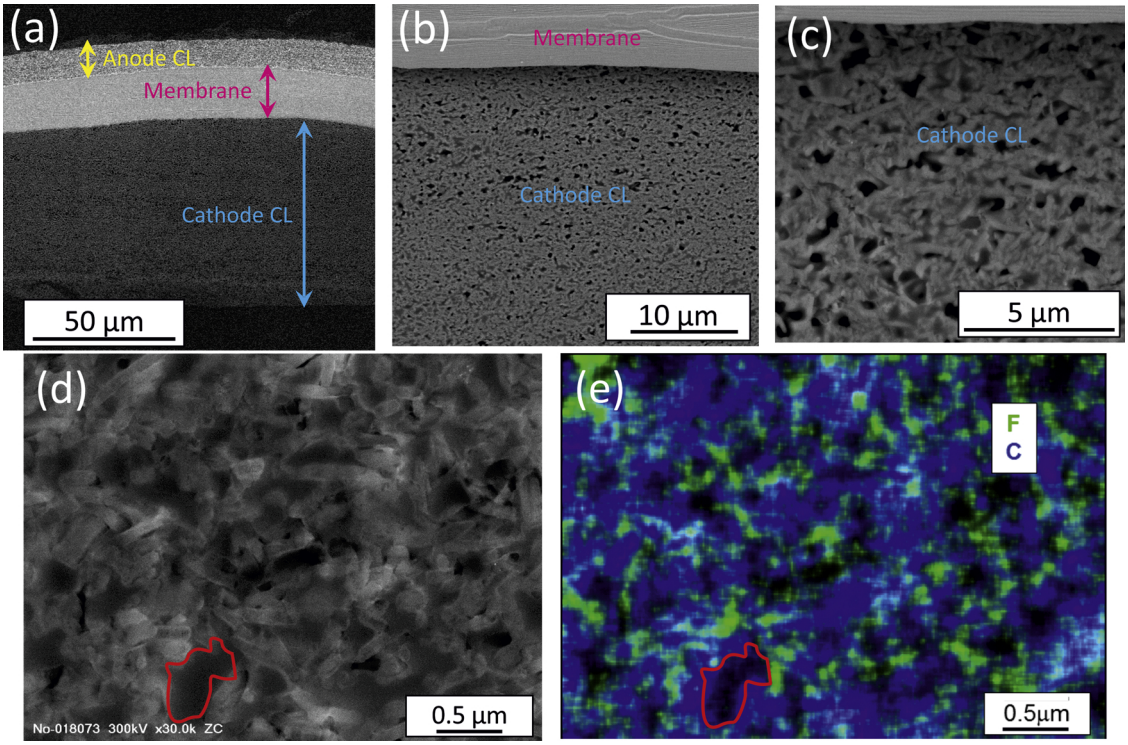

Fig. 2. (a) Cross-section SEM image of MEA showing Pt/C anode catalyst layer (top), N211 membrane, and (AD)Fe-N-C cathode catalyst layer (bottom). (b)-(c) SEM images at different magnification showing details of cathode catalyst layer structure. (d) HAADF-STEM image of cathode catalyst layer cross-section. (e) Fluorine and carbon overlaid EDS map of same area shown in (d). The red outline in (d) and (e) mark an example of a macropore (For interpretation of the references to colour in this figure legend, the reader is referred to the web version of this article).

process, the lack of a holistic study, as was performed for Pt-based MEAs [66], leaves a dearth of information on the subject on which to make a truly informed decision.

Nevertheless, the initial chronoamperometry results shown in Fig. 3a for MEA #0 (green line) indicated a sharp increase in performance over the first three hours (from 0.5 A cm^{-2} to *ca.* 1.1 A cm^{-2}). This was followed by a more moderate increase over the next hour to a current density of *ca.* 1.2 A cm^{-2}, after which the performance

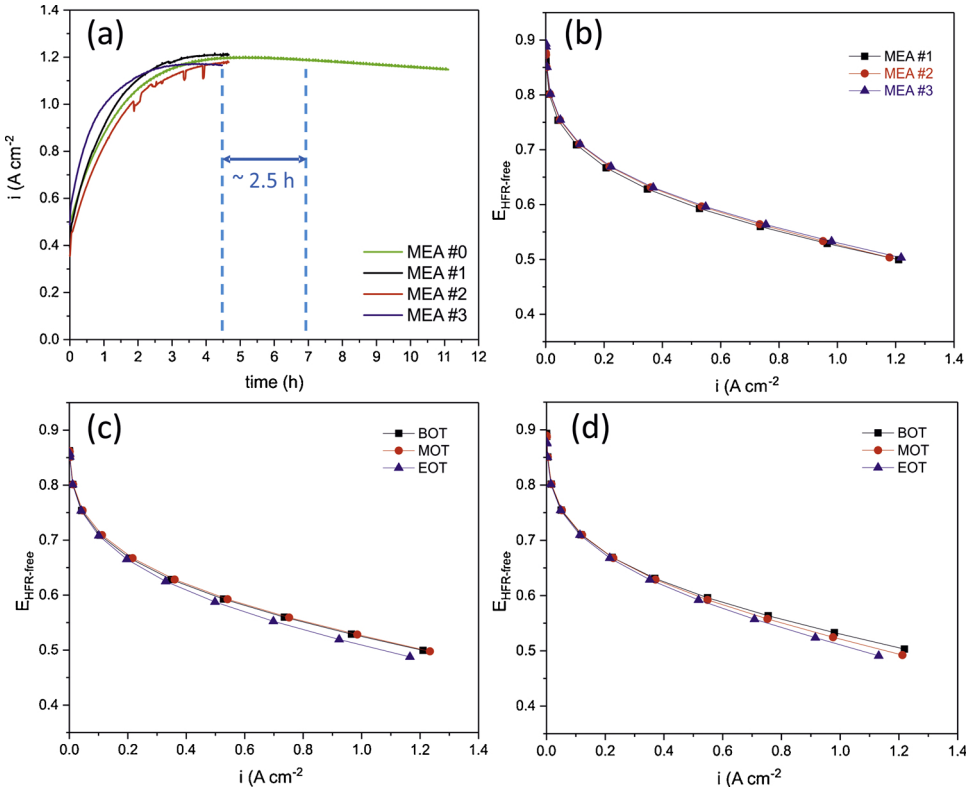

Fig. 3. (a) MEAs break-in protocol (constant 0.40 V, H_2/O_2, 80 °C, 1.5 atm) showing the timeframe where the catalyst is assumed stable and polarization curves were recorded. (b) BOT HFR-free polarization curves for three different MEAs (H_2/O_2, 80 °C, 1.5 atm). (c) BOT, MOT, and EOT polarization curves for MEA#1. (d) BOT, MOT, and EOT polarization curves for MEA#3.

appeared to stabilize for a short time before decreasing at an approximately constant rate.

From the initial chronoamperometry results of MEA #0, an activation time of 4.5 h was chosen to ensure that the MEA had indeed reached a plateau in its beginning-of-life performance. Ensuing repeats on additional MEAs (#1-3 in Fig. 3a) showed repeatable behavior comparable to that of MEA #0. Immediately following the 4.5 h break-in process, polarization curves (80 °C, H_2/O_2, 100% RH and P_{total} = 1.5 atm) were obtained for MEAs #1-3. These results were corrected for high frequency resistance (R_Ω^{HFR}, determined by AC impedance and comprised of membrane protonic (R_Ω^m) and cell bulk electronic and contact resistances, (R_Ω^e) – shown in Eqs. 1 and 2) and are displayed in Fig. 3b. The results indicate the excellent reproducibility of the (AD)Fe-N-C based electrodes at the beginning of test (BOT).

$$E_{HFR-free} = E_{cell} + i \cdot R_\Omega^{HFR} \quad (1)$$

$$R_\Omega^{HFR} = R_\Omega^m + R_\Omega^e \quad (2)$$

The acquisition of data necessary for the calculation of kinetic parameters such as exchange current density, reaction order and activation energy, required a time frame of about 2.5 h (highlighted with blue dashed lines in Fig. 3a) according to our desired testing protocols (see Table 1 and details in the Appendix – *Experimental*). While negligible or modest degradation was observed in this time frame during the potential hold for MEA #0, it is prudent to place internal standards throughout the protocol to ensure that the collected polarization data were suitable to properly determine the ORR kinetic parameters.

Polarization curves measured at 80 °C, 100% RH, and 1.5 atm were recorded immediately after the break-in at the BOT, in the middle-of-test (MOT) and at the end-of-test (EOT). Figs. 3c and d show the polarization data at the BOT, MOT and EOT for MEAs #1 and #3, respectively. While the order of data acquisition for MEAs #1 and #3 was varied (see Table 1) to compensate for the convolution of time/performance degradation in the subsequent analysis, the resulting spread of performance from the BOT to EOT polarization curves was similar. The consistency of the polarization curves for both MEAs is particularly evident at low current densities, where performance is typically limited by the ORR kinetics. Thus, we can conclude that the (AD)Fe-N-C catalyst does not undergo significant degradation within the testing protocol time frame and such issues will not complicate the subsequent kinetic analysis and any resulting conclusions. For polarization curves measured at different temperatures, according to the testing protocol for the determination of the activation energy indicated in Table1, please see Appendix – Fig. A.1.

Fig. 3 (a) MEAs break-in protocol (constant 0.40 V, H_2/O_2, 80 °C, 1.5 atm) showing the timeframe where the catalyst is assumed stable and polarization curves were recorded. (b) BOT HFR-free polarization curves for three different MEAs (H_2/O_2, 80 °C, 1.5 atm). (c) BOT, MOT, and EOT polarization curves for MEA#1. (d) BOT, MOT, and EOT polarization curves for MEA#3.

The polarization curves from step 3 to step 7 in Table 1 for MEAs #1, 2 and 3 are reported in Fig. 4a as *iR*-free cell potential (E_C), after correction for the high frequency (R_Ω^{HFR}) and cathode catalyst layer proton resistances, according to Eqs. 1 and 3.

$$E_C = E_{HFR-free} + i \bullet R_\Omega^C \quad (3)$$

The proton resistance in the cathode catalyst layer, derived from the EIS data shown in Fig. 4b, was calculated using a distributed kinetic model and previously established methods [67,68]. The accuracy of this correction is critical due to a near order of magnitude difference in thickness for typical PGM-free electrode layers vs. those for Pt-based electrocatalysts (*ca.* 100 µm vs. *ca.* 10 µm respectively) [5,69]. A proposed method for the quantification of the cathode catalyst layer proton resistance is described in several publications [67,70]. Briefly, EIS data acquired under a H_2/N_2 atmosphere (see Appendix – *Experimental*) is represented in the complex-plane (Nyquist plot) resulting in a purely capacitive response at the low frequencies in Fig. 4b. The intercept of this line with the real axis, less the real impedance at zero imaginary resistance (HFR), represents the H^+ resistance per geometric area of electrode (R_{sheet}), divided by 3 [68]. However, this has been proved to be a correct approximation only in the case where catalyst utilization is greater than 90%. Consequently, a correction factor (ζ) must be included to compensate for the distribution of the reaction current, and the expression of the proton resistance in the cathode catalyst layer (R_Ω^C) is described by Eq. (4) [29,68].

$$R_\Omega^C = \frac{R_{sheet}}{3 + \zeta} \quad (4)$$

The method for calculation of the correction factor ζ is described in detail in the work of Neyerlin et al. [27], and was also used here to produce the completely *iR*-free polarization curves in Fig. 4a.

Keeping in mind that the data for MEA #3 was collected in the reverse order of that for MEAs #1 and #2, evident once again is the very good reproducibility across all three MEAs. Only the data collected at 4.0 atm (*i.e.* p_{O2} = 3.5 atm) on MEA #3 varies in any amount from the other data sets, perhaps due to its earlier chronological acquisition relative to the data collected for MEAs #1 and #2.

Fig. 4 (a) *iR*-free polarization curves measured at 80 °C, 100% RH, and different pressures on MEAs #1, 2 and 3. (b) EIS measured at 80 °C, 1.5 atm, 100% RH on MEAs #1, 2 and 3. (c) Average *iR*-free polarization curves calculated from (a). (d) Average *iR*-free polarization curves corrected for thermodynamic contributions of H_2 and O_2 partial pressures.

This disparity notwithstanding, the polarization curves measured for the three different MEAs were then averaged (Fig. 4c), and finally corrected for the thermodynamic contributions of H_2 and O_2 partial pressure (Fig. 4d), according to Eq. 5.

$$E_{corr} = E_C - \frac{2.303RT}{4F}\log\left[\left(\frac{p_{H_2}}{p^*_{H_2}}\right)^2\left(\frac{p_{O_2}}{p^*_{O_2}}\right)\right] \quad (5)$$

Assuming negligible anodic overpotential [6], and the absence of oxygen mass transport resistance, the polarization curves in Fig. 4c-d only contain the cathode activation losses contribution. Thus, they can be used to calculate the ORR kinetic parameters.

Table 1
Testing protocols for the measurement of ORR kinetic parameters: reaction order and activation energy.

Testing protocol	Reaction order for MEAs # 1 and 2	Reaction order for MEA # 3	Activation Energy
Test conditions	H_2/O_2, 80 °C, 100% RH	H_2/O_2, 80 °C, 100% RH	H_2/O_2, 1.5 atm, 100% RH
Step 1	Break-in 0.40 V *ca.* 4.5 h	Break-in 0.40 V *ca.* 4.5 h	Break-in 0.40 V *ca.* 4.5 h
Step 2	Pol. curve 1.5 atm (BOT)	Pol. curve 1.5 atm (BOT)	Pol. curve 80 °C
Step 3	Pol. curve 1.0 atm	Pol. curve 4.0 atm	Pol. curve 70 °C
Step 4	Pol. curve 1.50 atm (MOT)	Pol. curve 3.0 atm	Pol. curve 60 °C
Step 5	Pol. curve 2.0 atm	Pol. curve 2.0 atm	
Step 6	Pol. curve 3.0 atm	Pol. curve 1.5 atm (MOT)	
Step 7	Pol. curve 4.0 atm	Pol. curve 1.0 atm	
Step 8	Pol. curve 1.5 atm (EOT)	Pol. curve 1.5 atm (EOT)	

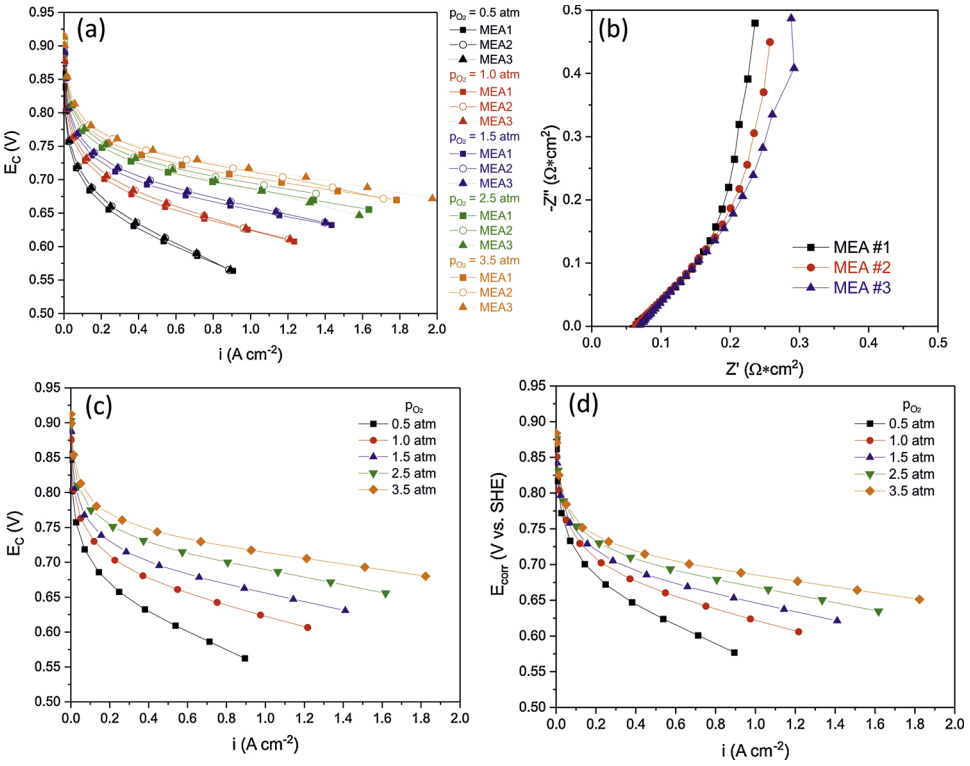

Fig. 4. (a) *iR*-free polarization curves measured at 80 °C, 100% RH, and different pressures on MEAs #1, 2 and 3. (b) EIS measured at 80 °C, 1.5 atm, 100% RH on MEAs #1, 2 and 3. (c) Average *iR*-free polarization curves calculated from (a). (d) Average *iR*-free polarization curves corrected for thermodynamic contributions of H_2 and O_2 partial pressures.

2.3. ORR kinetics modelling

At present, ORR kinetic studies for PGM-free catalysts have only been performed at the RDE level, where mass transport resistance limits the acquisition of kinetic information at low potential [44,52,54,71,72]. This is a critical point, since recent studies on PGM-free catalysts coupling RDE experiments with XANES analysis point to a potential-dependent availability of the ORR active sites for O_2 adsorption [39,45,46,57]. This availability or effectiveness (activity) has been attributed to a change in the oxidation state of the transition metal-based active sites, *e.g.*, from Fe^{3+} to Fe^{2+}. When the oxidation state of the Fe is high, adsorbed −OH species are postulated to limit O_2 adsorption, while when the oxidation state is low, −OH species are released, and the site becomes available for the adsorption of molecular oxygen, which is subsequently reduced [39,43,46,57]. In this context, the reaction turnover is vastly improved and the term "availability" can be used synonymously with a normalized activity. Nevertheless, assuming that the ORR rate-determining step remains the same, involving a single electron (n = 1) and proton transfer to the adsorbed O_2 molecule to generate an adsorbed −OOH intermediate, and the cathodic symmetry factor (β) is 0.5, the expected ORR Tafel slope should be 120–140 mV per decade (depending on temperature) [24]. The lower Tafel slope observed near OCV (60–70 mV per decade, see Appendix – Fig. A.2) is explained by a Nernstian behavior of the active-site-availability/activity term (θ), previously described in the literature, shown in Eq. (6) [39,43,46,52,57].

$$\theta = \frac{1}{1 + e^{\frac{F}{RT}(E_c^0 - E_R^0)}} \tag{6}$$

In prior works, the mathematical expression of θ has been proposed to be an exponential function of the cathode potential E_c^0 vs. SHE, $E_c^0 = E_C - (2.303RT/2F)\log p_{H_2}$, and potential of the reversible redox couple for ORR active sites (E_R^0). The basic assumption in this expression is that the total oxidation state change of the ORR active sites in the redox state transition is equal to 1. This assumption was made surmising a full net electron transition from and to the Fe-based catalytic center during the redox transition (*i.e.*, $Fe^{3+} \rightleftarrows Fe^{2+}$). However, due to the coordination of atomically-dispersed Fe atoms with other moieties (*e.g.* pyridinic and pyrrolic nitrogen) the net change in oxidation state of the active site, or distribution of active sites, is likely to have a non-integer value. This ligand effect would likely result in the distribution of any transferred charge across the extended active site complex. For this reason, a variable representing the effective change of the metal (in this case, Fe) oxidation state for the distribution of PGM-free active sites (n_R) must be included, as in Eq. (7).

$$\theta = \frac{1}{1 + e^{\frac{n_R F}{RT}(E_c^0 - E_R^0)}} \tag{7}$$

With this in mind, the cathode kinetic overpotential (η_C) can be described as shown in Eq. (8), where i_0^* is the catalyst electrode exchange current density (encapsulating the electrode loading as well as catalyst active site density and activity distribution), γ is the kinetic reaction order with respect to oxygen partial pressure (as defined in Eq. (9)), and ΔH_C is the activation energy of the ORR determined at zero overpotential (as defined in Eq. 10). It is important to reiterate, that while θ is often described as an active site availability, it is perhaps equally, if not more, reasonable to conceptualize θ as influencing active site activity, similarly to oxygen partial pressure or temperature in Eq. (8). Regardless, the argument as to whether θ is viewed as an availability or an activity modifier is a physiological and/or semantical one, since mathematically the influence of θ would be the same.

$$\eta_C = \frac{2.303RT}{\alpha_C F}\log\left(\frac{i}{i_0^* \cdot \left(\frac{p_{O_2}}{p_{O_2}^*}\right)^{\gamma} \cdot \theta \cdot \exp\left(-\frac{\Delta H_C}{R}\left(\frac{1}{T} - \frac{1}{T^*}\right)\right)}\right) \tag{8}$$

$$\gamma = \left(\frac{\partial \log i}{\partial \log p_{O_2}}\right)_{\eta_C, T} = \left(\frac{\partial \log i_0}{\partial \log p_{O_2}}\right)_T \tag{9}$$

$$-\Delta H_C = 2.303 \cdot R\left(\frac{\partial \log i_0}{\partial 1/T}\right)_{\eta=0, p_{O_2}} \tag{10}$$

According to Eq. (7), active site availability/activity reaches one when the cathode potential is sufficiently low, *i.e.,* cathode overpotential is sufficiently high. For these conditions, a Tafel slope of 120–140 mV per decade (depending on temperature) is expected. Consequently, as a first step, the completely *i*R-free polarization curve data was fit at high cathode overpotentials, > 500 mV, to obtain the catalyst electrode exchange current density at full availability/activity ($i_{0,T^*}^{\theta=1}$) for the various p_{O_2} values. This was done using the simple Tafel relation in Eq. (11), a simplification of Eq. (8) when θ = 1, and T = 80 °C, and is shown in Fig. 5a. Here, the linear dependence of the cathodic overpotential on the logarithm of the current density is consistent across the range of oxygen partial pressures examined, *ca.* 140 mV, as discussed earlier.

$$\eta_C = \frac{2.303RT}{\alpha_C F}\log\left(\frac{i}{i_{0,T^*}^{\theta=1}}\right) \tag{11}$$

To determine the catalyst exchange current density at full availability/activity at different temperatures ($i_0^{\theta=1}$, function of T), the same procedure was repeated for polarization curves acquired at various temperatures using Eq. (12)(see Table 1 "activation energy protocol" and Appendix – Figs. A.1a-d for polarization data).

$$\eta_C = \frac{2.303RT}{\alpha_C F}\log\left(\frac{i}{i_{0,p_{O2}}^{\theta=1}}\right) \tag{12}$$

Fig. 5 (a) Fitting of logarithm of current density as function of cathode kinetic overpotential with simple Tafel kinetic (Eq. 11) to extract $i_{0,T^*}^{\theta=1}$ values; data measured at 80 °C and 100% RH. (b) Fitting of γ and i_0^* with Eq. (13); data measured at 80 °C and 100% RH. (c) Fitting of ΔH_C with Eq. (14); data measured at 1.5 atm and 100% RH. (d) Fitting of n_R and E_R^0 with Eq. (16); data measured at 80 °C and 100% RH.

The resulting values for $i_{0,T^*}^{\theta=1}$ and $i_0^{\theta=1}$ are shown in Fig. 5b and c, respectively. Values of $i_{0,T^*}^{\theta=1}$ were then used in combination with Eq. (13) to extract the reaction order (γ) and the exchange current density at reference conditions (i_0^*) of; $p_{O_2}^* = 1$ atm, T* = 80 °C and 100% active site availability/activity.

$$i_{0,T^*}^{\theta=1} = i_0^* \bullet \left(\frac{p_{O_2}}{p_{O_2}^*}\right)^{\gamma} \tag{13}$$

Of note in Fig. 5b is the good agreement between the three $i_{0,T^*}^{\theta=1}$ values plotted when $p_{O_2} = 1$ atm, obtained from the BOT, MOT and EOT polarization curves. From Eq. (13), γ was found to be = 0.74 and $i_0^* = 59\ \mu A\ cm^{-2}$. The kinetic reaction order is similar to what has been determined for Pt-based electrocatalysts having utilized oxide dependent kinetics (γ≈ 0.7) [16], though results from experiments having a more limited cell operating potential (> 0.75 V), which utilized simple Tafel kinetics, yielded slightly lower values (γ≈ 0.55) [15,16].

With values for γ and i_0^* now established, the ORR activation energy at zero overpotential (ΔH_C, defined in Eq. 10) can be determined from Eq. (14).

$$i_{0,p_{O2}}^{\theta=1} = i_0^* \exp\left(-\frac{\Delta H_C}{R}\left(\frac{1}{T} - \frac{1}{T^*}\right)\right) \tag{14}$$

Fig. 5c shows the $i_{0,p_{O2}}^{\theta=1}$ values calculated at different temperatures (after correcting for variations in reactant partial pressure), plotted vs inverse temperature. The fitting results provided a ΔH_C value of 61.8 kJ mol^{-1}. This value is again similar to that for Pt/C-based electrocatalysts where the ORR activation energy values (55–77 kJ mol^{-1}), determined at zero overpotential, were extracted from MEA-level data [15,73,74].

With all necessary parameters extracted, focus now shifts to the determination of active site availability/activity as a function of potential and the elucidation of values for both n_R and E_R^0. Using Eq. (15), θ was calculated from the experimental polarization curve data and the results are plotted in Fig. 5d (symbols).

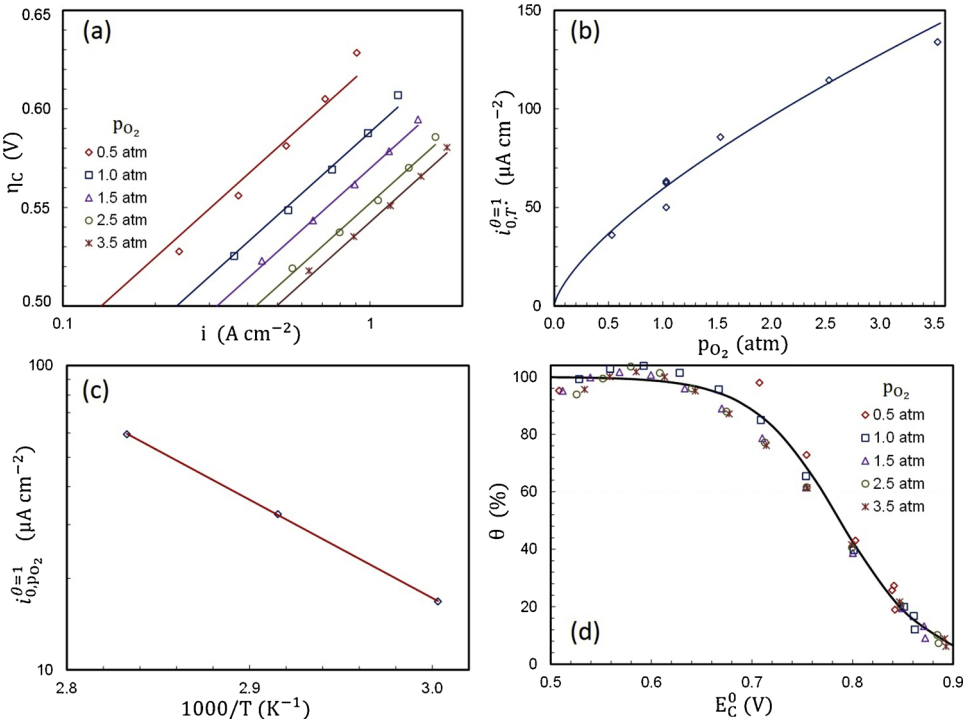

Fig. 5. (a) Fitting of logarithm of current density as function of cathode kinetic overpotential with simple Tafel kinetic (Eq. 11) to extract $i_{0,T^*}^{\theta=1}$ values; data measured at 80 °C and 100% RH. (b) Fitting of γ and i_0^* with Eq. (13); data measured at 80 °C and 100% RH. (c) Fitting of ΔH_C with Eq. 14; data measured at 1.5 atm and 100% RH. (d) Fitting of n_R and E_R^0 with Eq. 16; data measured at 80 °C and 100% RH.

$$\theta = \frac{i}{i_0^* \bullet \left(\frac{p_{O_2}}{p_{O_2}^*}\right)^{\gamma} \exp\left(\frac{\alpha_C F (E_{rev} - E_C)}{RT}\right)} \quad (15)$$

In Fig. 5d, the availability/activity of active sites in this PGM-free electrocatalyst is less than 10% near OCV. In addition, after the requisite corrections for thermodynamics and kinetics have been made, the effect of p_{O_2} on active site availability/activity appears negligible across the potential window and oxygen partial pressures examined here. The lone exception to this trend is the steeper increase of θ near cathode potentials of *ca.* 0.75 V for the data measured at low pressures (0.5 and 1.0 atm), which would need to be validated with additional studies. The dependence of θ on p_{O_2} has been reported for Pt-based catalysts. Here, θ would represent the fraction of the Pt surface free from oxide species that block O_2 adsorption [75]. For Pt-based catalysts, it has been reported in the literature that, when θ is pressure dependent, the apparent reaction order is smaller than the actual intrinsic reaction order for O_2 (expected to be equal to 1) [10], and θ is expected to be lower at high p_{O_2} and high temperature [24]. No studies regarding the pressure and temperature dependence of active site availability have been conducted so far on PGM-free catalysts. However, one can infer that the mechanism of this potential-dependent availability could be similar to the potential-dependent removal of the oxides from Pt surface, thus explaining the similarities between the behavior of PGM-free and Pt-based catalysts in this regard. Nevertheless, the black sigmoidal line in Fig. 5d represents a best fit curve for θ as a function of E_C, as in Eq. (7). Here, n_R and E_R^0 were allowed to be fit freely and found to be 0.712 and 0.787 V respectively.

2.4. Experimental validation of n_R and E_R^0

The fitted values of n_R and E_R^0 from the kinetic model were validated by determining the oxidation state of the Fe as a function of cathode potential. To that end, Fe XANES spectra for an (AD)Fe-N-C cathode of an MEA were acquired with helium on the cathode and hydrogen on the anode. Fig. 6a shows the Fe K-edge XANES spectra of the (AD)Fe-N-C catalyst at different potentials in one of the MEAs utilized earlier to acquire polarization data. To determine the effect of cathode potential on the oxidation state of Fe in the (AD)Fe-N-C catalyst, the spectra of two reference compounds, FeO and Fe(III)-phthalocyanine, were used to represent the oxidation states Fe^{+2} and Fe^{3+}, respectively. Iron oxide was used instead of Fe(II)-phthalocyanine because the XANES region of Fe(II) phthalocyanine exhibits strong pre-edge feature imparted by its square planar geometry which distorts its edge energy and XANES region. The comparison of edge energy with that of standards has been reported in the literature to calculate the Fe oxidation state in different Fe-containing compounds [76]. From Fig. 6a, it can be seen that, generically speaking, the XANES spectrum edge energy of the (AD) Fe-N-C catalyst progresses from a higher energy to a lower energy, indicative of a decrease in the oxidation state of the Fe, as the cell potential is decreased. To more accurately assess the progression of the change in oxidation state as well as establish a value for n_R, linear combination fitting of the XANES regions to that of the Fe^{2+} and Fe^{3+} standards was performed. Specifically, the XANES regions of the spectra (−20 eV to 30 eV versus the edge energy) for the two standards (FeO and Fe(III)-phthalocyanine) are combined at weighted fractions to minimize the difference between the calculated and experimental (AD) Fe-N-C spectra(AD)Fe-N-C. Subsequently, the Fe^{2+} and Fe^{3+} fractions were multiplied by their oxidation states, to obtain the potential dependent oxidation state plot in Fig. 6b.

Fig. 6 (a) *In situ* XANES spectra of (AD)Fe-N-C MEA cathode collected between 1.0 and 0.1 V. Data was collected at 80 °C, 100% RH, 1.5 atm with H_2/He flows at the anode/cathode respectively. (b) Fe oxidation states as a function of the cathode potential, calculated by linear combination fitting of XANES spectra of (AD)Fe-N-C catalysts and reference state compounds shown in (a). (c) CV of cathode of MEAs #1-2-3 measured at 20 mV s^{-1}. Data was collected at 80 °C, 100% RH, 1.5 atm with H_2/N_2 flows at the anode/cathode respectively. (d) CV of MEA #1, on which data from (a) and (b) were acquired (measured at 20 mV s^{-1}), superimposed with Fe oxidation state values from (b). The CV from (d) was obtained after the acquisition of the polarization data in Table 1 and concurrent with the XANES data. Data was collected at 80 °C, 100% RH, 1.5 atm with H_2/He flows at the anode/cathode respectively.

From Fig. 6a, the XANES edge energy shows a decrease between the 800 and 750 mV spectra and an approximately constant edge energy

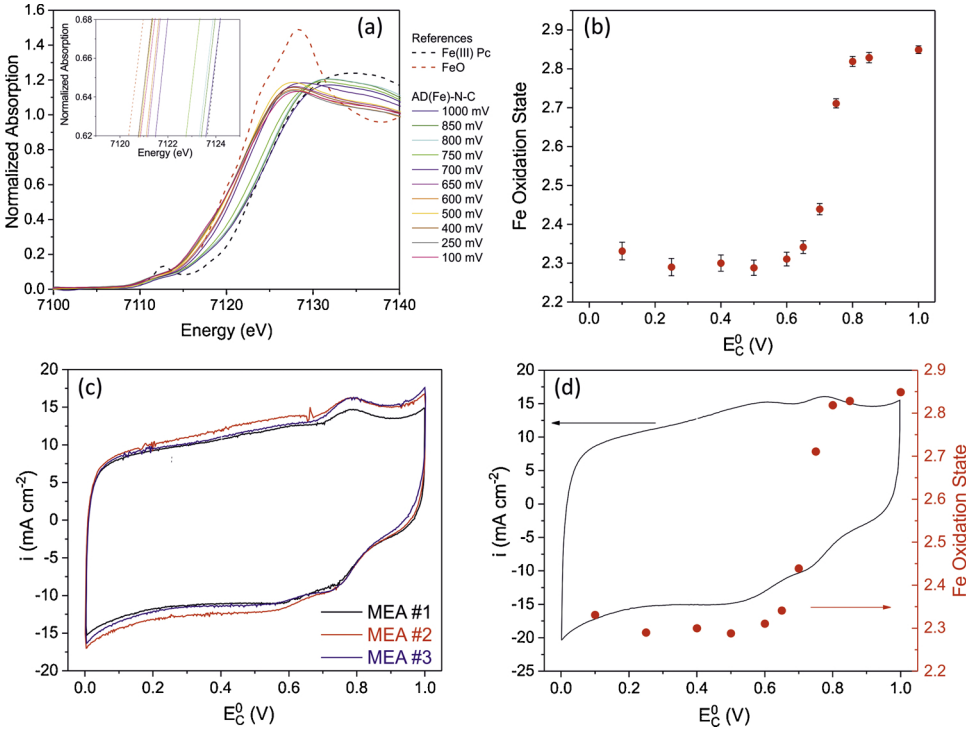

Fig. 6. (a) *In situ* XANES spectra of (AD)Fe-N-C MEA cathode collected between 1.0 and 0.1 V. Data was collected at 80 °C, 100% RH, 1.5 atm with H_2/He flows at the anode/cathode respectively. (b) Fe oxidation states as a function of the cathode potential, calculated by linear combination fitting of XANES spectra of (AD) Fe-N-C catalysts and reference state compounds shown in (a). (c) CV of cathode of MEAs #1-2-3 measured at 20 mV s^{-1}. Data was collected at 80 °C, 100% RH, 1.5 atm with H_2/N_2 flows at the anode/cathode respectively. (d) CV of MEA #1, on which data from (a) and (b) were acquired (measured at 20 mV s^{-1}), superimposed with Fe oxidation state values from (b). The CV from (d) was obtained after the acquisition of the polarization data in Table 1 and concurrent with the XANES data. Data was collected at 80 °C, 100% RH, 1.5 atm with H_2/He flows at the anode/cathode respectively.

at < 650 mV, as illustrated more clearly in the XANES linear combination fitting results shown in Fig. 6b. The midpoint between the highest oxidation state and the lowest oxidation state derived from Fig. 6b, 0.74 V, corresponds to the E_R^0 for the Fe redox reaction. The potentials over which the XANES data show a change in Fe oxidation state correspond well with the potentials of the redox peaks in the CVs of MEAs #1, 2 and 3, shown in Fig. 6c. For all the MEAs, a redox peak in the potential range between 0.75 and 0.80 V is present in both the anodic and cathodic scans. All the information gleaned from Figs. 6a-c aligns very well with the results from the kinetic model, where a value of 0.787 V was obtained for E_R^0. It is worth noting that similar redox peaks for Fe-based PGM-free catalysts were observed in CVs from both RDE and MEA experiments [39,44,45,77], and these redox peak potentials were demonstrated to have a strong correlation with the ORR onset potential [45,64,78–80].

On another note, from Fig. 6b, it is also evident that $n_R \neq 1$, *i.e.,* the Fe oxidation state transition is not from 3 to 2, but from *ca.* 2.85 to *ca.* 2.28. Thus, from *in situ* XANES data, $n_R \approx$ 0.57 for the (AD)Fe-N-C catalyst in a PEFC environment. This value is in the range of the results provided in the kinetic model above, where n_R was found to be significantly lower than 1 ($\approx$ 0.71). While variations in the oxidation state of Fe-based active sites from Fe^{3+} to Fe^{2+} have been previously observed as a function of cell potential using *in situ* XANES experiments [39,45,46,57], the oxidation state transition has never been used to model ORR kinetics, nor inserted in the exponential term, as in Eq. (7). The fractional (< 1) value of n_R can be envisioned as a partial charge transfer, attributable to the coordination of the Fe atom with N, or other ligands, and possibly with other species (*e.g.* OH* adsorbates) at high potentials. [45,60,63] One can assume an $n_R < 1$ as if the electric charge that is transferred during the redox transition does not completely transfer to the d-orbitals of the Fe atom, but it is partially shared with the surrounding atoms (Fe coordinated N or another adsorbed species).

As with data from any PGM-free electrocatalyst, it is important to recognize that all data obtained here potentially, and likely for that matter, encompasses a distribution of both active site types and activities. As a result, the kinetic information gleaned from any PGM-free electrocatalyst should be viewed in that context, until electrocatalysts with singular / model active sites can be synthesized. To that end, it is also possible that while the polarization data, by definition, only includes data from sites capable of facilitating the ORR, the XANES data would include information from any Fe species present in the sample, regardless of its ability to facilitate the ORR.

While there have been multiple previous investigations of PGM-free ORR kinetics utilizing a RDE, to the best of our knowledge, this work represents the first study where the ORR kinetics were investigated in a MEA. In previous works, RDE polarization and Fe-XANES data were collected and fit using Eq. (6)(*i.e.* $n_R = 1$), despite its prediction of a more abrupt θ transition relative to the experimental results [39,57,81]. The exponential term in Eqs. (6 and 7), represents a "Nernstian" potential-dependent state (activation) of the active sites. According to the theory previously proposed in the literature, the number of available active sites is potential-dependent, giving rise to a Nernstian Tafel slope at high potentials (*ca.* 70 mV at 80 °C), where active site activation / activity is the limiting factor for the ORR. This is the case in Fig. A.2a when $E_c > ca.$ 0.70 V. At potentials closer to OCV, the fraction of active site availability / activity is negligible and the overpotential serves primarily to generate active sites, concomitantly lowering the activation energy of the ORR. A Tafel slope of 70 mV is observed at high voltages, despite the predicted Faradaic ORR Tafel slope of *ca.* 140 mV, which should appear assuming the most likely condition of $\alpha_C = 0.5$ for the ORR, implying a symmetry factor $\beta = 0.5$, and one electron transferred in the rate determining step (n = 1). The Faradaic Tafel slope is however observed at higher overpotentials, when θ approaches unity and all the active sites are activated and available to carry out the ORR. This is the case in Fig. A.2a when $E_c < ca.$ 0.7 V. A hypothetical electrocatalytic system with a potential-independent active site population would exhibit a uniform slope over the complete potential range. Note that a more detailed and extensive explanations of potential-dependent active site availability are given elsewhere [39,43,52].

Nevertheless, the inclusion of the effective change of the Fe oxidation state (n_R) is an important distinction between the results and discussion presented in this publication and those described previously. Fig. A.3a shows the influence of n_R on a fixed value of E_R^0. Here, when $n_R = 1$ (implying a $Fe^{3+} \rightleftarrows Fe^{2+}$ transition), a more abrupt transition of θ with E_C is observed, while for fractional values of n_R, the transition of θ is more gradual. Due to the nature of the suspected metal-based active sites for PGM-free electrocatalysts and the distribution of charge among its associated ligands, the type of transition metal (*e.g.* Fe, Co, Mn) [41,42], metal-N coordination [60,63,82], in-plane or out-of-plane configuration [83], and the presence of particular adjacent functional groups or doping atoms (*e.g.* B, S, O, P) [84,85], could be influential in modifying n_R, θ, and the overall performance. In addition to the relative change in oxidation state, it would make sense that the absolute value of the initial oxidation state at high potential plays a role in dictating electrochemical performance and, consequently, E_R^0, but is out of the scope of what has been proposed and examined in this work.

Fig. A.3b shows, for a fixed value of n_R, the potential influence of E_R^0 on catalyst activity. For example, at $E_C = 0.80$V, with a catalyst with an $E_R^0 = 0.70$V would have less than 10% activity / availability of active sites. As E_R^0 increases to 0.75, 0.80 and 0.85 V, θ increases to approximately 20, 50 and 80%, respectively. This relation between E_R^0 and the catalyst activity has been pointed out in several publications [39,49,64,80,86]. According to the plot in Fig. A.3b, one could conclude that to produce a very active catalyst, the ultimate goal is to increase E_R^0 as much as possible. This may be true to an extent, but, above a certain value having a higher E_R^0 may no longer improve the electrocatalytic activity. Because O_2-active site binding energy is related to the chemistry of the active site(s) and thus, to the E_R^0, the activity of electrocatalysts having a low E_R^0 are limited by too high an O_2 binding energy, and by the active site activation / activity dictated by θ, while those with a higher E_R^0 are limited by a weak O_2 binding energy, which leads to more prominent H_2O_2 generation [43,49,64,82]. As a result, there will be an optimal E_R^0, at which the value of the O_2 adsorption energy is optimal, and θ is no longer a limiting factor, but active site density remains the major challenge.

Through the procedure described in Section 2.3 – *ORR Kinetics Modelling*, values for the kinetic parameters of the ORR on an (AD)Fe-N-C catalyst were calculated and are summarized in Table 2. Substitution of these values into Eqs. (4,7,8 and 17), and their ensuing incorporation into Eq. (16), results in an overall description of the ORR kinetics on the (AD)Fe-N-C electrocatalyst examined in this work.

$$E_{cell} = E_{rev} - i(R_\Omega^m + R_\Omega^e + R_\Omega^C) - \eta_C - \eta_A \quad (16)$$

$$E_{rev} = E_{rev}^0 + \frac{2.303RT}{4F}\log\left(\frac{p_{H_2}}{p_{H_2}^0}\right)^2\left(\frac{p_{O_2}}{p_{O_2}^0}\right) \quad (17)$$

The resulting kinetic model (solid lines) is plotted along with the experimental polarization data (open symbols) measured at different oxygen pressures in Fig. 7a and cell temperatures (Fig. 7b). The kinetic model provides an excellent fit of all the experimental data

Table 2
Summary of ORR Kinetic Data.

Parameter	Value	Unit
α_C	0.5	–
i_0^*	59.3 ± 5.8	μA cm^{-2}
γ	0.74 ± 0.05	–
ΔH_C	61.8	kJ mol^{-1}
E_R^0	0.787	V
n_R	0.71	–

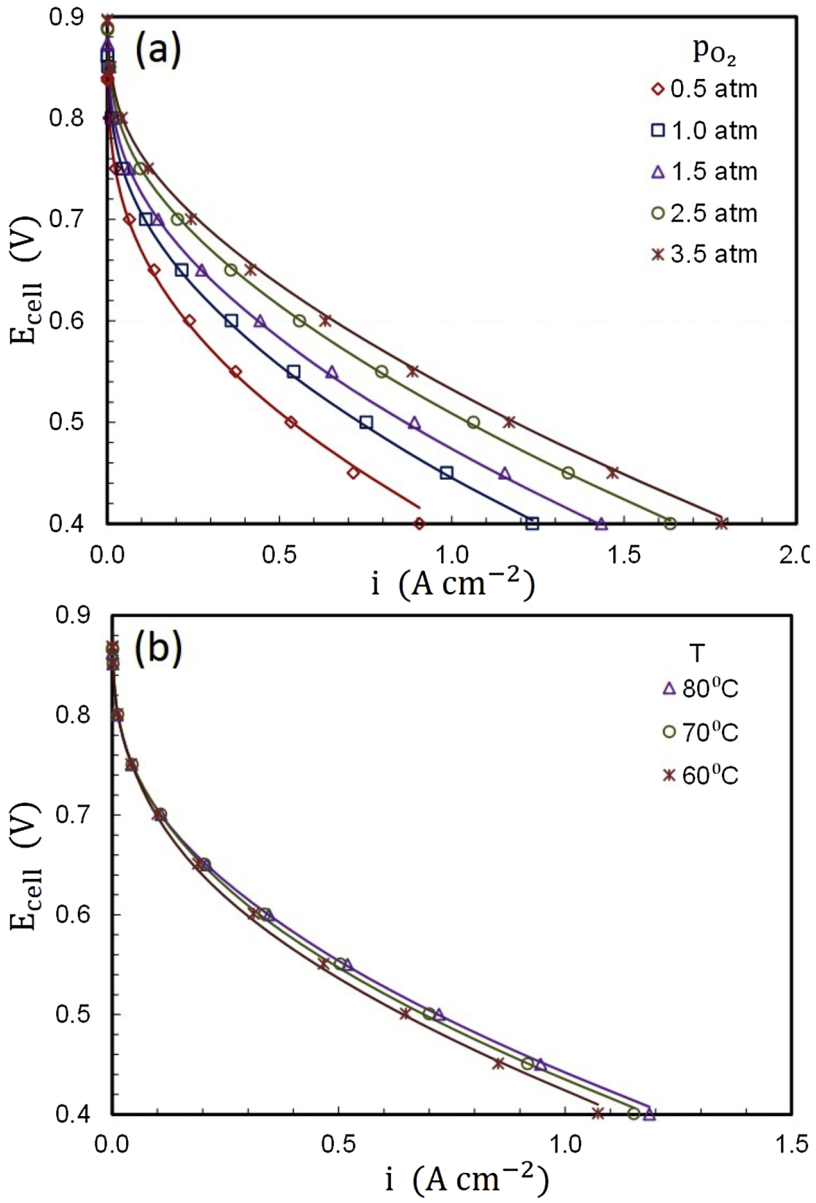

Fig. 7. (a) Kinetic modeling fitting (continuous lines) of experimental raw polarization curves (open bullet symbols) measured at 80 °C and 100% RH at different pressures. (b) Kinetic modeling fitting (continuous lines) of experimental raw polarization curves (open bullet symbols) measured at 1.5 atm and 100% RH at different temperatures.

simultaneously from OCV down to 0.40 V, across the complete range of p_{O_2} and T for which the experimental data are available. Moreover, since the model results in a near perfect agreement from low current density, dominated by kinetic phenomena, to high current density (> 1 A cm^{-2}), any concern about mass transport losses should be alleviated.

Fig. 7 (a) Kinetic modeling fitting (continuous lines) of experimental raw polarization curves (open bullet symbols) measured at 80 °C and 100% RH at different pressures. (b) Kinetic modeling fitting (continuous lines) of experimental raw polarization curves (open bullet symbols) measured at 1.5 atm and 100% RH at different temperatures.

3. Conclusions

A protocol for the extraction of the reaction order and the activation energy was designed and implemented for multiple MEAs incorporating an (AD)Fe-N-C cathode catalyst. Subsequently, the average polarization data at each potential, oxygen partial pressure, and temperature, were used to obtain values for the exchange current density (i_o), reaction order with respect to oxygen partial pressure (γ) and activation energy (ΔH_C). The values of these electrochemical parameters were then used to obtain a potential-dependent descriptor for the availability/activity of the ORR active sites (θ), which in turn was shown to be a function of the change in oxidation state for the Fe-based active sites (n_R) as well as the reversible redox potential for the distribution of active sites (E_R^0).

The values obtained for n_R and E_R^0 from model fitting agree well with the values determined experimentally by XANES and cyclic voltammetry, respectively. When the potential-dependent descriptor for active sites is incorporated into the electrochemical model, it results in an excellent fit over the entire range of operando data. The ORR kinetics on this (AD)Fe-N-C catalyst can be explained by the limited availability of active sites at low overpotentials. At high overpotentials, where all the active sites are available to carry out the ORR, the kinetics follow predicted Tafel behavior.

Pending operando stability, a framework has been established to enable the collection of MEA-level kinetic data for PGM-free electrocatalysts. For future work, the applicability of this kinetic model to

other PGM-free electrocatalysts, both Fe-based and non-Fe-based (*e.g.*, Co, Mn), will be examined. Further development between the relationship of the PGM-free active site complex, its observed redox potential, and the effective change in oxidation state, as well as the resulting kinetic performance, will be critical to improving the understanding and development of PGM-free electrocatalysts.

Declarations of interest

None.

Acknowledgments

This work was authored in part by Alliance for Sustainable Energy, LLC, the manager and operator of the National Renewable Energy Laboratory for the U.S. Department of Energy (DOE) under Contract No. DE-AC36-08GO28308. Research performed as part of the Electrocatalysis Consortium (ElectroCat), established as part of the Energy Materials Network, which is supported by the U.S. Department of Energy, Office of Energy Efficiency and Renewable Energy, Fuel Cell Technologies Office (FCTO). Microscopy performed as part of a user project at Oak Ridge National Laboratory's Center for Nanophase Materials Sciences, which is a U.S. Department of Energy, Office of Science User Facility. This research used resources of the Advanced Photon Source (APS), a U.S. Department of Energy (DOE) Office of Science User Facility operated for the DOE Office of Science by Argonne National Laboratory under Contract DE-AC02-06CH11357. The authors wish to thank Evan Wegener and Nancy Kariuki for their assistance setting up the X-ray absorption experiments as well as Dimitrios Papageorgopoulos and Simon Thompson in FCTO at DOE.

Appendix A. Supplementary data

Supplementary material related to this article can be found, in the online version, at doi:https://doi.org/10.1016/j.apcatb.2019.117929.

References

[1] H. Li, Y. Tang, Z. Wang, Z. Shi, S. Wu, D. Song, J. Zhang, K. Fatih, J. Zhang, H. Wang, Z. Liu, R. Abouatallah, A. Mazza, A review of water flooding issues in the proton exchange membrane fuel cell, J. Power Sources 178 (2008) 103–117, https://doi.org/10.1016/j.jpowsour.2007.12.068.

[2] Y.-J. Wang, D.P. Wilkinson, J. Zhang, Noncarbon support materials for polymer electrolyte membrane fuel cell electrocatalysts, Chem. Rev. 111 (2011) 7625–7651, https://doi.org/10.1021/cr100060r.

[3] Z. Chen, D. Higgins, A. Yu, L. Zhang, J. Zhang, A review on non-precious metal electrocatalysts for PEM fuel cells, Energy Environ. Sci. 4 (2011) 3167–3192, https://doi.org/10.1039/c0ee00558d.

[4] G. Wu, C.M. Johnston, N.H. Mack, K. Artyushkova, M. Ferrandon, M. Nelson, J.S. Lezama-Pacheco, S.D. Conradson, K.L. More, D.J. Myers, P. Zelenay, Synthesis–structure–performance correlation for polyaniline–Me–C non-precious metal cathode catalysts for oxygen reduction in fuel cells, J. Mater. Chem. 21 (2011) 11392–11405, https://doi.org/10.1039/c0jm03613g.

[5] H.A. Gasteiger, S.S. Kocha, B. Sompalli, F.T. Wagner, Activity benchmarks and requirements for Pt, Pt-alloy, and non-Pt oxygen reduction catalysts for PEMFCs, Appl. Catal. B Environ. 56 (2005) 9–35, https://doi.org/10.1016/j.apcatb.2004.06.021.

[6] D. Banham, S. Ye, Current status and future development of catalyst materials and catalyst layers for proton exchange membrane fuel cells: an industrial perspective, ACS Energy Lett. 2 (2017) 629–638, https://doi.org/10.1021/acsenergylett.6b00644.

[7] A. Kongkanand, M.F. Mathias, The priority and challenge of high-power performance of low-platinum proton-exchange membrane fuel cells, J. Phys. Chem. Lett. 7 (2016) 1127–1137, https://doi.org/10.1021/acs.jpclett.6b00216.

[8] B.N. Grgur, N.M. Marković, P.N. Ross, Temperature-dependent oxygen electrochemistry on platinum low-index single crystal surfaces in acid solutions, Can. J. Chem. 75 (1997) 1465–1471, https://doi.org/10.1017/CBO9781107415324.004.

[9] U.A. Paulus, A. Wokaun, G. Scherer, T.J. Schmidt, V. Stamenkovic, V. Radmilovic, N.M. Markovic, P.N. Ross, Oxygen reduction on carbon-supported Pt - Ni and Pt - Co alloy catalysts, J. Phys. Chem. B 106 (2002) 4181–4191, https://doi.org/10.1021/jp013442l.

[10] U.A. Paulus, T.J. Schmidt, H.A. Gasteiger, R.J. Behm, Oxygen reduction on a high-surface area Pt/Vulcan carbon catalyst: a thin-film rotating ring-disk electrode study, J. Electroanal. Chem. Lausanne (Lausanne) 495 (2001) 134–145, https://doi.org/10.1016/S0022-0728(00)00407-1.

[11] N.M. Markovic, T.J. Schmidt, B.N. Grgur, H.A. Gasteiger, R.J. Behm, P.N. Ross, Effect of temperature on surface processes at the Pt (111) - liquid interface : hydrogen adsorption, oxide formation, and CO oxidation, J. Phys. Chem. B 103 (1999) 8568–8577, https://doi.org/10.1021/jp991826u.

[12] V. Stamenković, T.J. Schmidt, P.N. Ross, N.M. Marković, Surface composition effects in electrocatalysis: kinetics of oxygen reduction on well-defined Pt 3 Ni and Pt 3 Co alloy surfaces, J. Phys. Chem. B 106 (2002) 11970–11979, https://doi.org/10.1021/jp021182h.

[13] A.M. Gómez-Marín, R. Rizo, J.M. Feliu, Some reflections on the understanding of the oxygen reduction reaction at Pt(111), Beilstein J. Nanotechnol. 4 (2013) 956–967, https://doi.org/10.3762/bjnano.4.108.

[14] M.L. Perry, Mass transport in Gas-Diffusion electrodes: a diagnostic tool for fuel-cell cathodes, J. Electrochem. Soc. 145 (1998) 5–15, https://doi.org/10.1149/1.1838202.

[15] K.C. Neyerlin, W. Gu, J. Jorne, H.A. Gasteiger, Determination of catalyst unique parameters for the oxygen reduction reaction in a PEMFC, J. Electrochem. Soc. 153 (2006) A1955, https://doi.org/10.1149/1.2266294.

[16] N.P. Subramanian, T.A. Greszler, J. Zhang, W. Gu, R. Makharia, Pt-oxide coverage-dependent oxygen reduction reaction (ORR) kinetics, J. Electrochem. Soc. 159 (2012) B531, https://doi.org/10.1149/2.088205jes.

[17] M. Shao, Q. Chang, J.-P. Dodelet, R. Chenitz, Recent advances in electrocatalysts for oxygen reduction reaction, Chem. Rev. 116 (2016) 3594–3657, https://doi.org/10.1021/acs.chemrev.5b00462.

[18] F. Jaouen, E. Proietti, M. Lefèvre, R. Chenitz, J.-P. Dodelet, G. Wu, H.T. Chung, C.M. Johnston, P. Zelenay, Recent advances in non-precious metal catalysis for oxygen-reduction reaction in polymer electrolyte fuel cells, Energy Environ. Sci. 4 (2011) 114–130, https://doi.org/10.1039/c0ee00011f.

[19] R. Othman, A.L. Dicks, Z. Zhu, Non precious metal catalysts for the PEM fuel cell cathode, Int. J. Hydrogen Energy 37 (2012) 357–372, https://doi.org/10.1016/j.ijhydene.2011.08.095.

[20] ElectroCat - Electrocatalysis Consortium - PGM-free electrocatalysts for next-generation fuel cells, (n.d.). https://www.electrocat.org/ (Accessed 7 January 2019).

[21] CRESCENDO - Critical Raw material ElectrocatalystS replaCement ENabling Designed pOst-2020 PEMFC, (n.d.). http://www.crescendo-fuelcell.eu/index.php (Accessed 7 January 2019).

[22] S.T. Thompson, A.R. Wilson, P. Zelenay, D.J. Myers, K.L. More, K.C. Neyerlin, D. Papageorgopoulos, ElectroCat: DOE's approach to PGM-free catalyst and electrode R&D, Solid State Ion. 319 (2018) 68–76, https://doi.org/10.1016/j.ssi.2018.01.030.

[23] E.J. Coleman, A.C. Co, The complex inhibiting role of surface oxide in the oxygen reduction reaction, ACS Catal. 5 (2015) 7299–7311, https://doi.org/10.1021/acscatal.5b02122.

[24] S. Gottesfeld, Some Observations on the Oxygen Reduction Reaction (ORR) At Platinum Catalysts based on Post Year 2000 Reports, ECS Trans. 6 (2008) 51–67, https://doi.org/10.1149/1.2943224.

[25] N.M. Markovic, T.J. Schmidt, V. Stamenkovic, P.N. Ross, Oxygen reduction reaction on Pt and Pt bimetallic surfaces: a selective review, Fuel Cells Weinh. (Weinh) 1 (2001) 105–116, https://doi.org/10.1002/1615-6854(200107)1:2<105::aid-fuce105>3.3.co;2-0.

[26] E.L. Redmond, B.P. Setzler, F.M. Alamgir, T.F. Fuller, Elucidating the oxide growth mechanism on platinum at the cathode in PEM fuel cells, Phys. Chem. Chem. Phys. 16 (2014) 5301–5311, https://doi.org/10.1039/c3cp54740j.

[27] K.C. Neyerlin, W. Gu, J. Jorne, A. Clark, H.A. Gasteiger, Cathode catalyst utilization for the ORR in a PEMFC, J. Electrochem. Soc. 154 (2007) B279, https://doi.org/10.1149/1.2400626.

[28] A. Holewinski, S. Linic, Elementary mechanisms in electrocatalysis: revisiting the ORR Tafel Slope, J. Electrochem. Soc. 159 (2012) H864–H870, https://doi.org/10.1149/2.022211jes.

[29] K.C. Neyerlin, H.A. Gasteiger, C.K. Mittelsteadt, J. Jorne, W. Gu, Effect of relative humidity on oxygen reduction kinetics in a PEMFC, J. Electrochem. Soc. 152 (2005) A1073, https://doi.org/10.1149/1.1897368.

[30] D.R. Baker, D.A. Caulk, K.C. Neyerlin, M.W. Murphy, Measurement of oxygen transport resistance in PEM fuel cells by limiting current methods, J. Electrochem. Soc. 156 (2009) B991, https://doi.org/10.1149/1.3152226.

[31] Y. Wang, J. Li, Z. Wei, Recent progress of carbon-based materials in oxygen reduction reaction catalysis, ChemElectroChem. (2018) 1–12, https://doi.org/10.1002/celc.201701335.

[32] H.M. Barkholtz, D.-J. Liu, Advancements in rationally designed PGM-free fuel cell catalysts derived from metal–organic frameworks, Mater. Horizons 4 (2017) 20–37, https://doi.org/10.1039/C6MH00344C.

[33] J. Dodelet, The controversial role of the metal in Fe- or Co-based electrocatalysts for the oxygen reduction reaction, in: Acid Medium, M. Shao (Eds.), Electrocatal. Fuel Cells, Springer, London, London, 2013, pp. 271–338, , https://doi.org/10.1007/978-1-4471-4911-8.

[34] U.I. Kramm, J. Herranz, N. Larouche, T.M. Arruda, M. Lefèvre, F. Jaouen, P. Bogdanoff, S. Fiechter, I. Abs-Wurmbach, S. Mukerjee, J.-P. Dodelet, Structure of the catalytic sites in Fe/N/C-catalysts for O2-reduction in PEM fuel cells, Phys. Chem. Chem. Phys. 14 (2012) 11673–11688, https://doi.org/10.1039/c2cp41957b.

[35] J.-Y. Choi, L. Yang, T. Kishimoto, X. Fu, S. Ye, Z. Chen, D. Banham, Is the rapid initial performance loss of Fe/N/C non precious metal catalysts due to micropore flooding? Energy Environ. Sci. 10 (2017) 296–305, https://doi.org/10.1039/C6EE03005J.

[36] R. Chenitz, U.I. Kramm, M. Lefevre, V. Glibin, G. Zhang, S. Sun, J.-P. Dodelet, A specific demetalation of Fe-N4 catalytic sites in the micropores of NC_Ar + NH3 is at

the origin of the initial activity loss of this highly active Fe/N/C catalyst used for the reduction of oxygen in PEM fuel cell, Energy Environ. Sci. (2017) 1–30, https://doi.org/10.1039/C7EE02302B.
[37] G. Zhang, R. Chenitz, M. Lefèvre, S. Sun, J.P. Dodelet, Is iron involved in the lack of stability of Fe/N/C electrocatalysts used to reduce oxygen at the cathode of PEM fuel cells? Nano Energy 29 (2016) 111–125, https://doi.org/10.1016/j.nanoen.2016.02.038.
[38] H. Zhang, S. Hwang, M. Wang, Z. Feng, S. Karakalos, L. Luo, Z. Qiao, X. Xie, C. Wang, D. Su, Y. Shao, G. Wu, Single atomic Iron catalysts for oxygen reduction in acidic media: particle size control and thermal activation, J. Am. Chem. Soc. 139 (2017) 14143–14149, https://doi.org/10.1021/jacs.7b06514.
[39] J. Li, A. Alsudairi, Z.-F. Ma, S. Mukerjee, Q. Jia, Asymmetric volcano trend in oxygen reduction activity of Pt and non-Pt catalysts: in situ identification of the site-blocking effect, J. Am. Chem. Soc. 139 (2017) 1384–1387, https://doi.org/10.1021/jacs.6b11072.
[40] H.T. Chung, D.A. Cullen, D. Higgins, B.T. Sneed, E.F. Holby, K.L. More, P. Zelenay, Direct atomic-level insight into the active sites of a high-performance PGM-free ORR catalyst, Science 357 (80-) (2017) 479–484, https://doi.org/10.1126/science.aan2255.
[41] J. Li, M. Chen, D.A. Cullen, S. Hwang, M. Wang, B. Li, K. Liu, S. Karakalos, M. Lucero, H. Zhang, C. Lei, H. Xu, G.E. Sterbinsky, Z. Feng, D. Su, K.L. More, G. Wang, Z. Wang, G. Wu, Atomically dispersed manganese catalysts for oxygen reduction in proton-exchange membrane fuel cells, Nat. Catal. (2018) 1, https://doi.org/10.1038/s41929-018-0164-8.
[42] Y. He, S. Hwang, D.A. Cullen, M.A. Uddin, L. Langhorst, B. Li, S. Karakalos, A.J. Kropf, E.C. Wegener, J. Sokolowski, M. Chen, D.J. Myers, D. Su, K.L. More, G. Wang, S. Litster, G. Wu, Highly active atomically dispersed CoN4 fuel cell cathode catalysts derived from surfactant-assisted MOFs: carbon-shell confinement strategy, Energy Environ. Sci. (2019), https://doi.org/10.1039/C8EE02694G.
[43] S. Gottesfeld, Generation of active sites by potential-driven surface processes: a central aspect of electrocatalysis, ECS Trans. 61 (2014) 1–13, https://doi.org/10.1149/06131.0001ecst.
[44] J. Chlistunoff, RRDE and voltammetric study of orr on pyrolyzed fe / polyaniline catalyst. On the origins of variable Tafel Slopes, J. Phys. Chem. C 115 (2011) 6496–6507.
[45] U. Tylus, Q. Jia, K. Strickland, N. Ramaswamy, A. Serov, P. Atanassov, S. Mukerjee, Elucidating oxygen reduction active sites in pyrolyzed metal-nitrogen coordinated non-precious-metal electrocatalyst systems, J. Phys. Chem. C 118 (2014) 8999–9008, https://doi.org/10.1021/jp500781v.
[46] J. Li, S. Ghoshal, W. Liang, M.-T. Sougrati, F. Jaouen, B. Halevi, S. McKinney, G. McCool, C. Ma, X. Yuan, Z.-F. Ma, S. Mukerjee, Q. Jia, Structural and mechanistic basis for the high activity of Fe–N–C catalysts toward oxygen reduction, Energy Environ. Sci. 9 (2016) 2418–2432, https://doi.org/10.1039/C6EE01160H.
[47] H. Tributsch, U.I. Koslowski, I. Dorbandt, Experimental and theoretical modeling of Fe-, Co-, Cu-, Mn-based electrocatalysts for oxygen reduction, Electrochim. Acta 53 (2008) 2198–2209, https://doi.org/10.1016/j.electacta.2007.09.027.
[48] K. Tammeveski, J.H. Zagal, Electrocatalytic oxygen reduction on transition metal macrocyclic complexes for anion exchange membrane fuel cell application, Curr. Opin. Electrochem. (2018), https://doi.org/10.1016/j.coelec.2018.04.001.
[49] J.H. Zagal, M.T.M. Koper, Reactivity descriptors for the activity of molecular MN4 catalysts for the oxygen reduction reaction, Angew. Chem. Int. Ed. 55 (2016) 14510–14521, https://doi.org/10.1002/anie.201604311.
[50] J. Masa, A. Zhao, X. Wei, M. Muhler, W. Schuhmann, Metal-free catalysts for oxygen reduction in alkaline electrolytes: influence of the presence of Co, Fe, Mn and Ni inclusions, Electrochim. Acta 128 (2014) 271–278, https://doi.org/10.1016/j.electacta.2013.11.026.
[51] F. Jaouen, J.-P. Dodelet, O2 reduction mechanism on non-noble metal catalysts for PEM fuel cells. Part I: experimental rates of O2 electroreduction, H2O2 electroreduction, and H2O2 disproportionation, J. Phys. Chem. C 113 (2009) 15422–15432, https://doi.org/10.1021/jp900837.
[52] L. Osmieri, A.H.A. Monteverde Videla, P. Ocón, S. Specchia, Kinetics of oxygen electroreduction on Me-N-C (Me = Fe, Co, Cu) catalysts in acidic medium. Insights on the effect of the transition metal, J. Phys. Chem. C 121 (2017) 17796–17817, https://doi.org/10.1021/acs.jpcc.7b02455.
[53] L. Osmieri, R. Escudero-Cid, M. Armandi, P. Ocón, A.H.A. Monteverde Videla, S. Specchia, Effects of using two transition metals in the synthesis of non-noble electrocatalysts for oxygen reduction reaction in direct methanol fuel cell, Electrochim. Acta 266 (2018) 220–232, https://doi.org/10.1016/j.electacta.2018.02.036.
[54] F. Jaouen, V. Goellner, M. Lefèvre, J. Herranz, E. Proietti, J.P. Dodelet, Oxygen reduction activities compared in rotating-disk electrode and proton exchange membrane fuel cells for highly active FeNC catalysts, Electrochim. Acta 87 (2013) 619–628, https://doi.org/10.1016/j.electacta.2012.09.057.
[55] P. Zelenay, D.J. Myers, ElectroCat Project 2017 DOE Annual Merit Review, ElectroCat Proj, 2017 DOE Annu. Merit Rev, 2017 (Accessed 4 April 2018), https://hydrogendoedev.nrel.gov/pdfs/progress17/v_a_1_zelenay_2017.pdf.
[56] H.T. Chung, Atomically dispersed (AD)Fe-N-C oxygen reduction catalysts for polymer electrolyte fuel cells, Under Prep. (2019).
[57] Q. Jia, N. Ramaswamy, H. Hafiz, U. Tylus, K. Strickland, G. Wu, B. Barbiellini, A. Bansil, E.F. Holby, P. Zelenay, S. Mukerjee, Experimental observation of redox-induced Fe-N switching behavior as a determinant role for oxygen reduction activity, ACS Nano 9 (2015) 12496–12505, https://doi.org/10.1021/acsnano.5b05984.
[58] H. Zhang, H. Osgood, X. Xie, Y. Shao, G. Wu, Engineering nanostructures of PGM-free oxygen-reduction catalysts using metal-organic frameworks, Nano Energy 31 (2017) 331–350, https://doi.org/10.1016/j.nanoen.2016.11.033.
[59] X. Wang, X. Fan, H. Lin, H. Fu, T. Wang, J. Zheng, X. Li, An efficient Co–N–C oxygen reduction catalyst with highly dispersed Co sites derived from a ZnCo bimetallic zeolitic imidazolate framework, RSC Adv. 6 (2016) 37965–37973, https://doi.org/10.1039/C6RA04771H.
[60] E.F. Holby, G. Wu, P. Zelenay, C.D. Taylor, Structure of Fe−Nx−C defects in oxygen reduction reaction catalysts from first-principles modeling, J. Phys. Chem. C 118 (2014) 14388–14393.
[61] K. Artyushkova, A. Serov, S. Rojas-Carbonell, P. Atanassov, Chemistry of multitudinous active sites for oxygen reduction reaction in transition metal-nitrogen-Carbon electrocatalysts, J. Phys. Chem. C (2015), https://doi.org/10.1021/acs.jpcc.5b07653 acs.jpcc.5b07653.
[62] M. Lefèvre, E. Proietti, F. Jaouen, J.-P. Dodelet, Iron-based catalysts with improved oxygen reduction activity in polymer electrolyte fuel cells, Science 324 (80-) (2009) 71–74, https://doi.org/10.1126/science.1170051.
[63] E.F. Holby, P. Zelenay, Linking structure to function: the search for active sites in non-platinum group metal oxygen reduction reaction catalysts, Nano Energy 29 (2016) 54–64, https://doi.org/10.1016/j.nanoen.2016.05.025.
[64] J.H. Zagal, F. Javier Recio, C.A. Gutierrez, C. Zuñiga, M.A. Páez, C.A. Caro, Towards a unified way of comparing the electrocatalytic activity MN4 macrocyclic metal catalysts for O2 reduction on the basis of the reversible potential of the reaction, Electrochem. commun. 41 (2014) 24–26, https://doi.org/10.1016/j.elecom.2014.01.009.
[65] R. Chenitz, U.I. Kramm, M. Lefevre, V. Glibin, G. Zhang, S. Sun, J.-P. Dodelet, A specific demetalation of Fe-N4 catalytic sites in the micropores of NC_Ar + NH3 is at the origin of the initial activity loss of this highly active Fe/N/C catalyst used for the reduction of oxygen in PEM fuel cell, Energy Environ. Sci. (2017) 365–382, https://doi.org/10.1039/C7EE02302B.
[66] S. Kabir, G. Bender, W.E. Klein, S.S. Kocha, K.C. Neyerlin, Investigating the Effects of Catalyst Loading and MEA Conditioning on Commercial Pt/C and State-of-the-Art Pt-Alloy/C Performance in a PEMFC, 233rd ECS Meet, (2018) (Accessed 20 May 2018), https://ecs.confex.com/ecs/233/webprogram/Paper111014.html.
[67] G. Li, P.G. Pickup, Ionic conductivity of PEMFC electrodes, J. Electrochem. Soc. 150 (2003) C745, https://doi.org/10.1149/1.1611493.
[68] R. Makharia, M.F. Mathias, D.R. Baker, Measurement of catalyst layer electrolyte resistance in PEFCs using electrochemical impedance spectroscopy, J. Electrochem. Soc. 152 (2005) A970, https://doi.org/10.1149/1.1888367.
[69] S.S. Kocha, Principles of MEA preparation, in: W. Vielstich, A. Lamm, H.A. Gasteiger (Eds.), Handb. Fuel Cells – Fundam. Technol. Appl. John Wiley & Sons, Ltd, Chichester, 2003, pp. 538–565.
[70] E.B. Easton, P.G. Pickup, An electrochemical impedance spectroscopy study of fuel cell electrodes, Electrochim. Acta 50 (2005) 2469–2474, https://doi.org/10.1016/j.electacta.2004.10.074.
[71] L. Osmieri, R. Escudero-Cid, M. Armandi, A.H.A. Monteverde Videla, J.L.G. Fierro, P. Ocón, S. Specchia, Fe-N/C catalysts for oxygen reduction reaction supported on different carbonaceous materials. Performance in acidic and alkaline direct alcohol fuel cells, Appl. Catal. B Environ. 205 (2017) 637–653, https://doi.org/10.1016/j.apcatb.2017.01.003.
[72] L. Osmieri, R. Escudero-Cid, A.H.A. Monteverde Videla, P. Ocón, S. Specchia, Performance of a Fe-N-C catalyst for the oxygen reduction reaction in direct methanol fuel cell: cathode formulation optimization and short-term durability, Appl. Catal. B Environ. 201 (2017) 253–265, https://doi.org/10.1016/j.apcatb.2016.08.043.
[73] P.D. Beattie, V.I. Basura, S. Holdcroft, Temperature and pressure dependence of O2 reduction at Pt|Nafion® 117 and Pt|BAM® 407 interfaces, J. Electroanal. Chem. Lausanne (Lausanne) 468 (1999) 180–192, https://doi.org/10.1016/S0022-0728(99)00164-3.
[74] X. Wang, I.-M. Hsing, P.L. Yue, Electrochemical characterization of binary carbon supported electrode in polymer electrolyte fuel cells, J. Power Sources 96 (2001) 282–287, https://doi.org/10.1016/S0378-7753(00)00625-X.
[75] C.H. Paik, T.D. Jarvi, W.E. O'Grady, Extent of PEMFC cathode surface oxidation by oxygen and water measured by CV, Electrochem. Solid-State Lett. 7 (2004) A82, https://doi.org/10.1149/1.1649698.
[76] M. Ferrandon, X. Wang, A.J. Kropf, D.J. Myers, G. Wu, C.M. Johnston, P. Zelenay, Stability of iron species in heat-treated polyaniline–iron–carbon polymer electrolyte fuel cell cathode catalysts, Electrochim. Acta 110 (2013) 282–291, https://doi.org/10.1016/j.electacta.2013.03.183.
[77] F. Jaouen, J. Herranz, M. Lefèvre, J.-P. Dodelet, U.I. Kramm, I. Herrmann, P. Bogdanoff, J. Maruyama, T. Nagaoka, A. Garsuch, J.R. Dahn, T. Olson, S. Pylypenko, P. Atanassov, Ea. Ustinov, Cross-laboratory experimental study of non-noble-metal electrocatalysts for the oxygen reduction reaction, ACS Appl. Mater. Interfaces 1 (2009) 1623–1639, https://doi.org/10.1021/am900219g.
[78] J. Perez, E.R. Gonzalez, E.A. Ticianelli, Oxygen electrocatalysis on thin porous coating rotating platinum electrodes, Electrochim. Acta 44 (1998) 1329–1339.
[79] L. Birry, J.H. Zagal, J.P. Dodelet, Does CO poison Fe-based catalysts for ORR? Electrochem. commun. 12 (2010) 628–631, https://doi.org/10.1016/j.elecom.2010.02.016.
[80] N. Ramaswamy, S. Mukerjee, Fundamental mechanistic understanding of electrocatalysis of oxygen reduction on Pt and Non-Pt surfaces: acid versus alkaline media, Adv. Phys. Chem. 2012 (2012) 1–17, https://doi.org/10.1155/2012/491604.
[81] A. Alsudairi, J. Li, N. Ramaswamy, Resolving the Iron phthalocyanine redox transitions for ORR catalysis in aqueous media, J. Phys. Chem. Lett. 8 (2017) 2881–2886, https://doi.org/10.1021/acs.jpclett.7b01126.
[82] M. Busch, N.B. Halck, U. Kramm, S. Siahrostami, P. Krtil, J. Rossmeisl, Beyond the Top of the Volcano? A unified approach to electrocatalytic oxygen reduction and oxygen evolution, Nano Energy 29 (2016) 1–10, https://doi.org/10.1016/j.nanoen.2016.04.011.

[83] Q. Jia, N. Ramaswamy, U. Tylus, K. Strickland, J. Li, A. Serov, K. Artyushkova, P. Atanassov, J. Anibal, C. Gumeci, S.C. Barton, M.T. Sougrati, F. Jaouen, B. Halevi, S. Mukerjee, Spectroscopic insights into the nature of active sites in iron-nitrogen-carbon electrocatalysts for oxygen reduction in acid, Nano Energy 29 (2016) 65–82, https://doi.org/10.1016/j.nanoen.2016.03.025.

[84] C.H. Choi, S.H. Park, S.I. Woo, Binary and ternary doping of nitrogen, boron, and phosphorus into carbon for enhancing electrochemical oxygen reduction activity, ACS Nano 6 (2012) 7084–7091, https://doi.org/10.1021/nn3021234.

[85] J. Liang, Y. Jiao, M. Jaroniec, S.Z. Qiao, Sulfur and nitrogen dual-doped mesoporous graphene electrocatalyst for oxygen reduction with synergistically enhanced performance, Angew. Chem. Int. Ed. 51 (2012) 11496–11500, https://doi.org/10.1002/anie.201206720.

[86] X. Wang, Y. Liu, Y. Wang, R. Ren, H. Chen, Z. Jiang, Q. He, Electrochemical and spectroscopic study of homo- and hetero-dimetallic phthalocyanines as catalysts for the oxygen reduction reaction in acidic media, ChemElectroChem. (2018) 1–9, https://doi.org/10.1002/celc.201800977.